nature portfolio

https://doi.org/10.1038/s41928-021-00561-5

Supplementary information

High-mobility p-type semiconducting two-dimensional β-TeO_2

In the format provided by the authors and unedited

High mobility p-type semiconducting two-dimensional β-TeO_2

Ali Zavabeti,[a,b,§*] Patjaree Aukarasereenont,[a,§] Hayden Tuohey,[a] Nitu Syed, [a] Azmira Jannat,[c] Aaron Elbourne,[a] Kibret A. Messalea,[c] Bao Yue Zhang,[c] Billy J. Murdoch,[a] James G. Partridge,[a] Matthias Wurdack,[d] Daniel L Creedon,[e] Joel van Embden,[a] Kourosh Kalantar-Zadeh,[f] Salvy P. Russo,[a,g] Chris F. McConville,[a,h*] Torben Daeneke[c*]

[a] School of Science, RMIT University, Melbourne, VIC 3001, Australia

[b] Department of Chemical Engineering, The University of Melbourne, Parkville, VIC 3010, Australia

[c] School of Engineering, RMIT University, Melbourne, VIC 3001, Australia

[d] Nonlinear Physics Centre, Research School of Physics, The Australian National University,

Canberra, ACT 2601, Australia

[e] School of Physics, The University of Melbourne, Parkville, VIC 3010, Australia

[f] School of Chemical Engineering, University of New South Wales (UNSW), Kensington, NSW 2031, Australia

[g] ARC Centre of Excellence in Exciton Science, School of Science, RMIT University, Melbourne, VIC, 3001, Australia

[h] Institute for Frontier Materials, Deakin University, Waurn Ponds, Geelong, VIC 3216, Australia

[§]A. Z. and P.A. contributed equally.

Email: ali.zavabeti@unimelb.edu.au, chris.mcconville@deakin.edu.au, torben.daeneke@rmit.edu.au

Supplementary Information

Supplementary Note 1: Printing parameters

Additional experiments were performed to analyse the effects of printing parameters such as the rolling speed and droplet size on the transferred sheets and substrate coverage. It was observed that the maximum attainable rolling speed depends on the size of the droplet. Larger droplets tend to fragmentate when rolled too fast or separate from the glass rod, resulting in an upper printing speed limit. This behaviour is summarised in Extended Data Figure 1a. The oxidation time prior to rolling and its influence on the sheet thickness was also investigated. Extended Data Figure 1b shows that extending the growth time before rolling results in no significant increase in sheet thickness of the 2D TeO_2.

The degree of surface coverage depending on the printing speed was also investigated. A fast-continuous motion was found to lead to sparse surface coverage which may be preferred when individual flakes are to be synthesised for subsequent dry-transfer. A higher surface coverage was obtained when a step by step coating procedure was adopted. Here the droplet is allowed to oxidise for a set time, is moved the distance of one droplet diameter and is then allowed to re-oxidise for the same time period prior to being moved again. For this stepped roll-printing, the oxidation time per step was found to have profound effects on substrate coverage and lateral dimensions of the isolated sheets (Extended Data Figure 1c). When the droplets were rolled at relatively slower step-speeds, a substrate coverage exceeding 50% can be obtained. This may be improved upon in further work. Supplementary Information Movie S3 shows the result from a 3-minute oxidation-step experiment, leaving behind a large area that is covered with 2D TeO_2 sheets.

Supplementary Note 2: Hole effective mass measurement

Scanning tunnelling spectroscopy (STS) was employed to measure the tunnelling current at a constant distance from the sample. The tip bias and tunnelling current can be modelled using Fowler-Nordheim (Equation S1):[1]

$$I_t \propto U^2 \exp\left(\frac{8\pi\sqrt{2m^*}}{3ehU}\varphi^{3/2}z\right) \qquad \text{(Eq. S1)}$$

Where I_t and U represent the tunnelling current and tip bias, respectively. z is the gap between sample and tip, which was constant since the measurement was conducted under constant distance mode. h and e are Planck's constant and the unit of charge of an electron, respectively. m^* is the effective mass of the charge carrier, while φ is the barrier potential. Equation S1 can be simplified as below:[2,3]

$$I_t = \alpha_1 \times U^2 \exp\left(\alpha_2 \frac{\sqrt{m^*}}{U}\right) \qquad \text{(Eq. S2)}$$

The STS curve obtained was fitted into Equation S2 using MATLAB program R2019b. A curve fitting algorithm from the optimisation toolbox was used to obtain m_h^*. An effective mass of m_h^* = 0.51 was determined with the coefficient of determination being R^2 = 0.992, demonstrating an excellent fit (Extended Data Figure 6).

Supplementary Note 3: Field-effect mobility calculation

The field-effect mobilities at ambient and cryogenic temperatures were calculated using the relation:

$$\mu_p = \frac{dI_D}{dV_G}\frac{L}{WV_D C_{ox}} \qquad \text{(Eq. S3)}$$

Where μ_p is the hole mobility, I_D and V_D refer to the drain-source current and voltage, respectively, V_G is the gate voltage, L and W are the length and width of the channel, respectively, and C_{ox} is the gate insulator capacitance (9 nF cm^{-2} for thermally grown 300 nm SiO_2).

Supplementary Note 4: Resistivity measurements

The measurements, performed along the two principal axes of the device, resulted in the resistances R_{xx} = 445.3 kΩ and R_{xy} = 62.89 MΩ, and a van der Pauw anisotropy of:

$$A_{vdP} = \frac{R_{xx}}{R_{xy}} = 141.23 \qquad \text{(Eq. S4)}$$

The van der Pauw method ordinarily assumes a uniform, homogeneous and isotropic material. However, it has been demonstrated that the technique can also be used to accurately determine the properties of anisotropic materials.[4] The asymmetry in the resistance of the sample can be related to the real transport anisotropy through the analytically obtained expression:

$$A_{vdP} = \frac{R_{xx}}{R_{xy}} = \frac{\sum_{n=odd^+}[n\sinh(\sqrt{A_{eff}^{-1}}\pi n)]^{-1}}{\sum_{n=odd^+}[n\sinh(\sqrt{A_{eff}}\pi n)]^{-1}} \qquad \text{(Eq. S5)}$$

where A_{eff} is an effective anisotropy which combines the geometrical aspect ratio of the samples and the transport anisotropy. We prepared a square van der Pauw geometry and assumed that our contacts have an ideal aspect ratio of 1. Numerical solving from the Equation S5 resulted in A_{eff} = 4.18 and the resistivity of the sample along the two principal axes is then given by:

$$\rho_{xx} = \rho_{avg}\sqrt{A_{eff}^{-1}} \qquad \text{(Eq. S6)}$$

$$\rho_{yy} = \rho_{avg}\sqrt{A_{eff}} \qquad \text{(Eq. S7)}$$

where ρ_{avg} is the average resistivity determined by solving the van der Pauw equation normally used for isotropic samples:

$$\exp(-\pi \frac{R_{xx}}{\rho_{avg}}) + \exp(-\pi \frac{R_{yy}}{\rho_{avg}}) = 1 \qquad \text{(Eq. S8)}$$

From solving for ρ_{avg}, a sheet resistance R_S^{avg} = 53.91 MΩ/square can be obtained from $R_S^{avg} = \rho_{avg}$ x t (where t is the sample thickness). From this, the anisotropic sheet resistances of the two principal axes were determined by:

$$R_S^{xx} = R_S^{avg}\sqrt{A_{eff}^{-1}} = 26.37 \text{ MΩ/square} \qquad \text{(Eq. S9)}$$

$$R_S^{yy} = R_S^{avg}\sqrt{A_{eff}} = 110.23 \text{ MΩ/square} \qquad \text{(Eq. S10)}$$

Multiplying by the sample thickness in cm will provide the resistivity ρ in units of Ω.cm.

Supplementary Note 5: Charge carrier density and Hall mobility measurements

A DC magnetic field between -0.7 and +0.7 T was applied perpendicular to the sample surface. The longitudinal Hall voltage was then derived from:

$$V_{xy}(B) = \frac{\tilde{V}_{xy}(B) - \tilde{V}_{xy}(-B)}{2} \qquad \text{(Eq. S11)}$$

in which $\tilde{V}_{xy}(B)$ is the raw measured Hall voltage. The Hall voltage was then obtained by:

$$V_H = \frac{IB}{nte} \qquad \text{(Eq. S12)}$$

where I is the current, B is the magnetic field, n is the charge carrier density, t is the thickness of the sample, and e is the electron charge. According to the Equation S12, the charge carrier density is n_{2D} = 1.04 x 10^9 cm^{-2}. The anisotropic mobility of the sample can be calculated from:

$$\mu = \frac{1}{en\rho} = \frac{1}{n_{2D}R_S e} \qquad \text{(Eq. S13)}$$

This resulted in the following mobilities for the principal axes of the devices:

$$\mu_{xx} = 227.61 \text{ cm}^2/\text{Vs} \qquad \text{(Eq. S14)}$$

$$\mu_{yy} = 54.46 \text{ cm}^2/\text{Vs} \qquad \text{(Eq. S15)}$$

With the average mobility being μ_{avg} = 141 cm^2/Vs, which agrees well with measured FET mobilities μ_{FET} = 146 ± 42 cm^2/Vs.

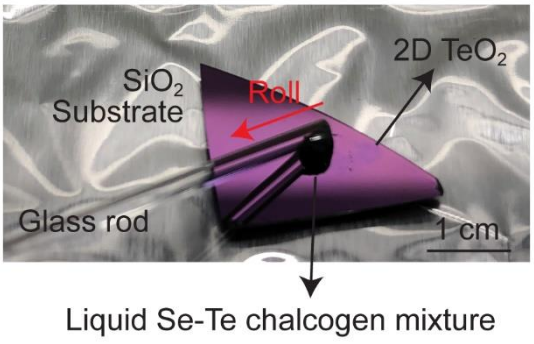

Supplementary Figure 1. Roll-transfer method. Surface oxides can be transferred via rolling of a Se/Te droplet on a SiO_2 300 nm/Si wafer. The transferred 2D TeO_2 is visible behind the droplet.

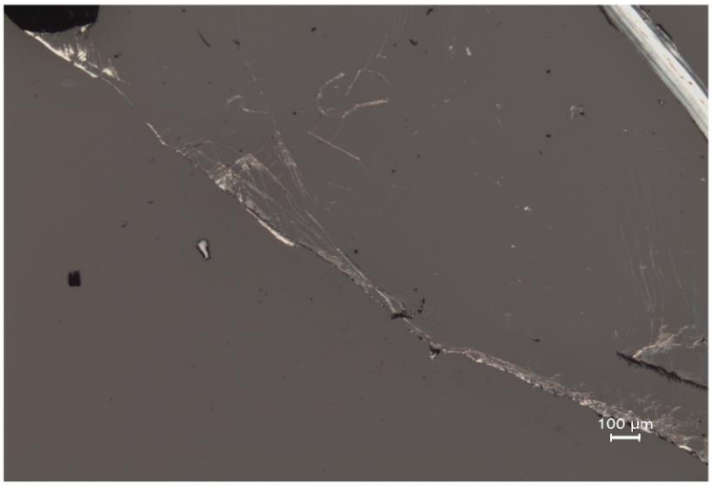

Supplementary Figure 2. Optical microscopy image of 2D TeO_2. A large area highly transparent 2D sheet was transferred onto a quartz substrate.

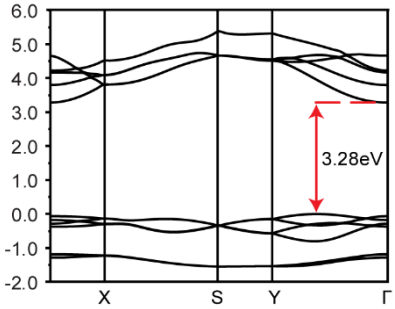

Supplementary Figure 3. Electronic Band Structure plot for bulk β-TeO_2. The indirect bandgap was predicted to be 3.28 eV.

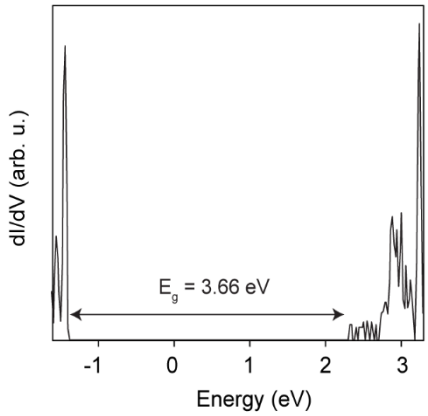

Supplementary Figure 4. Scanning tunnelling spectroscopy data for 2D TeO_2.

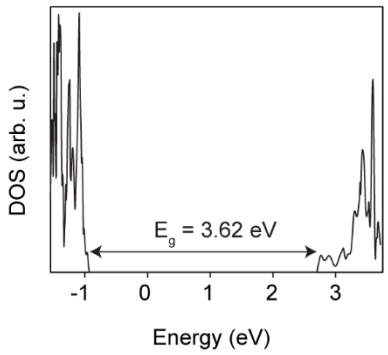

Supplementary Figure 5. Bilayer TeO_2 DOS. Calculated density of states for bilayer 2D TeO_2.

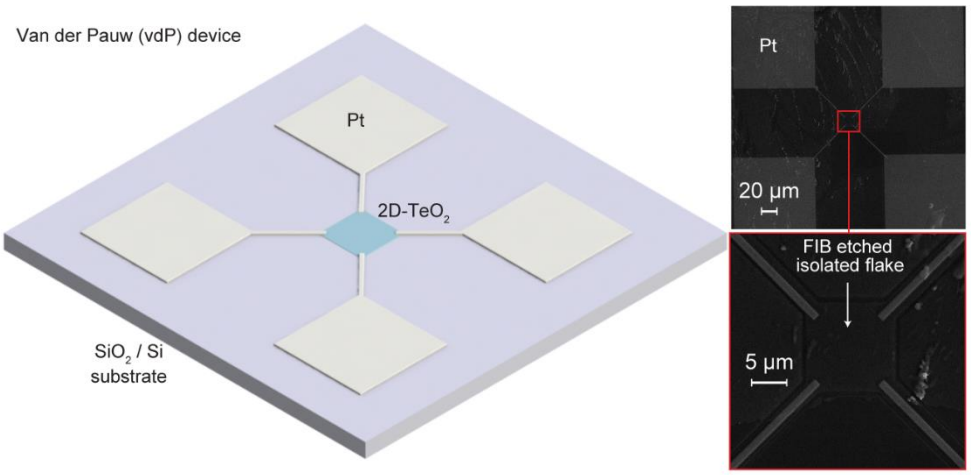

Supplementary Figure 6. Hall effect measurements. A schematic of the standard van der Pauw (vdP) device for Hall mobility measurements with SEM images.

Supplementary Table 1. Gibbs free energy of formation for oxides of both selenium and tellurium.

Chemical composition	Calculated ΔG_f kJ/mol	Reference
SeO_2	− 86.154	[5]
SeO_3	− 171.797	[5]
γ-TeO_2	−229.8	[6]
α-TeO_2	−232.8	[6]
β-TeO_2	−236.3	[6]

Supplementary Table 2. Selected reported FETs utilising p-type oxides as their channel material.

Oxides	E_g (eV)	μ ($cm^2V^{-1}s^{-1}$)	I_{on}/I_{off}	SS ($V\ dec^{-1}$)	Year	Reference
NiO	-	1.6×10^{-4}	130	-	2008	[7]
NiO	-	5.2	2.2×10^3	3.91	2013	[8]
NiO	3.41-3.7	0.05	10^3	2.6	2015	[9]
NiO_x	-	25.2 ± 1.7	10^5	0.7	2016	[10]
NiO_x	-	4.4	10^5	0.25	2016	[11]
NiO_x	3.65-3.82	0.78	5.3×10^4	1.37	2018	[12]
NiO	3.69-3.78	6.0	10^7	0.13	2019	[13]
Cu_2O	-	0.26	6.0	-	2008	[14]
CuO	1.41	0.4	10^4	-	2010	[15]
Cu_2O	-	2.4	3.96×10^4	-	2012	[16]
Cu_2O	-	0.06	10^4	3	2013	[17]
Cu_2O	-	0.16	10^2	-	2013	[18]
CuO	1.5	0.01	10^4	3.3	2014	[19]
CuO	-	0.78 ± 0.03	10^5	0.4	2015	[20]
Cu_xO	-	0.44 ± 0.05	$10^3 – 10^4$	5.2 ± 0.5	2016	[10]
Cu_2O	-	0.002	10^3	-	2016	[21]
CuO	-	0.01	10^3	-	2016	[21]
Cu_xO	-	2.7	2×10^5	0.19	2017	[22]
Cu_2O	2.36	5.2×10^{-4}	-	4.2	2018	[23]
CuO	1.55	2.33×10^{-4}	-	8	2018	[23]
Cu_xO	2.1-3.3	0.15	10^4	-	2019	[24]
SnO	2.7	1.3	10^2	-	2008	[25]
SnO	-	0.24	10^2	-	2010	[26]
SnO	2.78	1.8	1.3×10^3	-	2013	[27]
SnO	2.65-2.92	6.75	6×10^3	7.63-10	2013	[28]
SnO	2.8-2.95	1.9	-	-	2016	[29]
SnO	4.2	0.7	20	-	2017	[30]
SnO_x	2.6-2.75	4.6	7×10^4	-	2019	[31]
SnO	2.66	0.29 ± 0.07	$5.4 (\pm 0.2) \times 10^2$	11.9 ± 1.2	2019	[32]
$CuAlO_2$	3.24-3.8	0.1	10^3	8.6	2018	[33]
$CuAlO_2$	3.61-3.73	1.36	10^5	-	2019	[34]
$CuCrO_2$	2.95-3.02	0.59	10^5	5.66	2018	[35]
$Cu_{1-x}Cr_xO_{2-\delta}$	2.8	0.32	7×10^2	-	2014	[36]
β-TeO_2	3.7	232	10^6	0.103 ± 3	2020	This work

Supplementary Table 3. Selected reported FETs utilising n-type oxides as their channel material.

Oxides	E_g (eV)	μ ($cm^2V^{-1}s^{-1}$)	I_{on}/I_{off}	SS ($V\ dec^{-1}$)	Year	Reference
In_2O_3	3.65	~140	10^5	0.09	2006	[37]
In_2O_3	3.7-3.85	55.26	10^7	-	2011	[38]
In_2O_3	-	127	10^6	0.137	2013	[39]
In_2O_3	-	3.98	10^8	0.4	2013	[40]
In_2O_3	-	23.6	1.1×10^7	0.09	2014	[41]
In_2O_3	-	8	10^6	0.4	2015	[42]
In_2O_3	-	21.22	10^7	0.1	2019	[43]
SnO_2	-	2	10^5	4	2004	[44]
SnO_2	-	17.4	10^6	0.72	2009	[45]
SnO_2	-	103	$10^4 – 10^5$	0.3	2013	[46]
SnO_2	-	35.4	4.5×10^7	0.623	2015	[47]
SnO_2	~4	0.23	10^6	-	2017	[48]
SnO_2	-	7.3	10^6	1.25	2019	[49]
SnO_2	-	92	3×10^6	0.074	2019	[50]
SnO_2	3.6-4.1	0.511	2.3×10^4	5.06	2020	[51]
SnO_2	4.3	20	10^5	0.65 ± 0.02	2020	[52]
ZnO	-	1.2	10^6	-	2003	[53]
ZnO	-	20	2×10^5	1.24	2005	[54]
ZnO	3.31	5.25	1.65×10^5	-	2007	[55]
ZnO	-	11	10^7	1.78	2013	[56]
ZnO	-	20.2	10^7	~0.4	2015	[57]
ZnO	-	12.76	10^8	0.26	2020	[58]
ZnO	-	2.8	10^5	-	2020	[59]
ZnO	3.34	0.117	10^5	-	2020	[60]
IGZO	~3	7	10^3	-	2004	[61]
IGZO	-	12	10^8	0.2	2006	[62]
IGZO	-	3.3	7×10^7	0.18	2009	[63]
IGZO	-	61.5	10^5	0.61	2010	[64]
IGZO	-	76	6.7×10^5	0.129	2013	[65]
IGZO	-	9.1	10^6	0.22	2018	[66]

References

1 Müller-Meskamp, L. *et al.* Field-emission resonances at tip/α,ω-Mercaptoalkyl Ferrocene/Au interfaces studied by STM. *Small* **5**, 496-502, (2009).

2 Jannat, A. *et al.* Ordered-vacancy-enabled indium sulphide printed in wafer-scale with enhanced electron mobility. *Mater. Horiz.* **7**, 827-834, (2020).

3 Messalea, K. A. *et al.* Two-step synthesis of large-area 2D Bi_2S_3 nanosheets featuring high in-plane anisotropy. *Adv. Mater. Interfaces* **n/a**, 2001131, (2020).

4 Bierwagen, O., Pomraenke, R., Eilers, S. & Masselink, W. T. Mobility and carrier density in materials with anisotropic conductivity revealed by van der Pauw measurements. *Phys. Rev. B* **70**, 165307, (2004).

5 Olin, Å., Nolang, B., Osadchii, E. G., Öhman, L.-O. & Rsen, E. *Chemical thermodynamics of selenium*. Vol. 7 41 (Elsevier, 2005).

6 Ceriotti, M., Pietrucci, F. & Bernasconi, M. Ab initio study of the vibrational properties of crystalline TeO_2: The α, β and γ phases. *Phys. Rev. B* **73**, 104304, (2006).

7 Shimotani, H., Suzuki, H., Ueno, K., Kawasaki, M. & Iwasa, Y. P-type field-effect transistor of NiO with electric double-layer gating. *Appl. Phys. Lett.* **92**, 242107, (2008).

8 Jiang, J., Wang, X., Zhang, Q., Li, J. & Zhang, X. Thermal oxidation of Ni films for p-type thin-film transistors. *Phys. Chem. Chem. Phys.* **15**, 6875-6878, (2013).

9 Chen, Y. *et al.* Tunable electrical properties of NiO thin films and p-type thin-film transistors. *Thin Solid Films* **592**, 195-199, (2015).

10 Shan, F. *et al.* High-mobility p-type NiO_x thin-film transistors processed at low temperatures with Al_2O_3 high-k dielectric. *J. Mater. Chem. C* **4**, 9438-9444, (2016).

11 Liu, A. *et al.* Hole mobility modulation of solution-processed nickel oxide thin-film transistor based on high-k dielectric. *Appl. Phys. Lett.* **108**, 233506, (2016).

12 Hu, H., Zhu, J., Chen, M., Guo, T. & Li, F. Inkjet-printed p-type nickel oxide thin-film transistor. *Appl. Surf. Sci.* **441**, 295-302, (2018).

13 Xu, W. *et al.* P-type transparent amorphous oxide thin-film transistors using low-temperature solution-processed nickel oxide. *J. Alloys Compd.* **806**, 40-51, (2019).

14 Matsuzaki, K. *et al.* Epitaxial growth of high mobility Cu_2O thin films and application to p-channel thin film transistor. *Appl. Phys. Lett.* **93**, 202107, (2008).

15 Sung, S.-Y. *et al.* Fabrication of p-channel thin-film transistors using CuO active layers deposited at low temperature. *Appl. Phys. Lett.* **97**, 222109, (2010).

16 Yao, Z. Q. *et al.* Room temperature fabrication of p-channel Cu_2O thin-film transistors on flexible polyethylene terephthalate substrates. *Appl. Phys. Lett.* **101**, 042114, (2012).

17 Jeong, C.-Y. *et al.* Investigation of the charge transport mechanism and subgap density of states in p-type Cu_2O thin-film transistors. *Appl. Phys. Lett.* **102**, 082103, (2013).

18 Kim, S. Y. *et al.* P-channel oxide thin film transistors using solution-processed copper oxide. *ACS Appl. Mater. Interfaces* **5**, 2417-2421, (2013).

19 Sanal, K. C., Vikas, L. S. & Jayaraj, M. K. Room temperature deposited transparent p-channel CuO thin film transistors. *Appl. Surf. Sci.* **297**, 153-157, (2014).

20 Liu, A. *et al.* Water-induced scandium oxide dielectric for low-operating voltage n- and p-type metal-oxide thin-film transistors. *Adv. Funct. Mater.* **25**, 7180-7188, (2015).

21 Jang, J., Chung, S., Kang, H. & Subramanian, V. P-type CuO and Cu_2O transistors derived from a sol-gel copper (II) acetate monohydrate precursor. *Thin Solid Films* **600**, 157-161, (2016).

22 Liu, A. *et al.* In situ one-step synthesis of p-type copper oxide for low-temperature, solution-processed thin-film transistors. *J. Mater. Chem. C* **5**, 2524-2530, (2017).

23 Shijeesh, M. R. & Jayaraj, M. K. Low temperature fabrication of Cu_xO thin-film transistors and investigation on the origin of low field effect mobility. *J. Appl. Phys.* **123**, 161538, (2018).

24 Liu, A., Zhu, H. & Noh, Y. Y. Polyol reduction: a low temperature eco-friendly solution process for p-channel copper oxide-based transistors and inverter circuits. *ACS Appl. Mater. Interfaces* **11**, 33157-33164, (2019).

25 Ogo, Y. *et al.* P-channel thin-film transistor using p-type oxide semiconductor, SnO. *Appl. Phys. Lett.* **93**, 032113, (2008).

26 Yabuta, H. *et al.* Sputtering formation of p-type SnO thin-film transistors on glass toward oxide complimentary circuits. *Appl. Phys. Lett.* **97**, 072111, (2010).

27 Hsu, P. C. *et al.* Fabrication of p-type SnO thin-film transistors by sputtering with practical metal electrodes. *Jpn. J. Appl. Phys.* **52**, 05DC07, (2013).

28 Caraveo-Frescas, J. A. *et al.* Record mobility in transparent p-type tin monoxide films and devices by phase engineering. *ACS Nano* **7**, 5160-5167, (2013).

29 Saji, K. J., Tian, K., Snure, M. & Tiwari, A. 2D tin monoxide—an unexplored p-type van der Waals semiconductor: material characteristics and field effect transistors. *Adv. Electron. Mater.* **2**, 1500453, (2016).

30 Daeneke, T. *et al.* Wafer-scale synthesis of semiconducting SnO monolayers from interfacial oxide layers of metallic liquid tin. *ACS Nano* **11**, 10974-10983, (2017).

31 Barros, R. *et al.* Role of structure and composition on the performances of p-type tin oxide thin-film transistors processed at low-temperatures. *Nanomaterials* **9**, 320, (2019).

32 Yim, S. *et al.* Lanthanum doping enabling high drain current modulation in a p-type tin monoxide thin-film transistor. *ACS Appl. Mater. Interfaces* **11**, 47025-47036, (2019).

33 Li, S. *et al.* Preparation and characterization of solution-processed nanocrystalline p-type $CuAlO_2$ thin-film transistors. *Nanoscale Res. Lett.* **13**, 259, (2018).

34 Wang, C. *et al.* Sol–gel processed p-type $CuAlO_2$ semiconductor thin films and the integration in transistors. *IEEE Trans. Electron Devices* **66**, 1458-1463, (2019).

35 Nie, S. *et al.* Solution-processed ternary p-type $CuCrO_2$ semiconductor thin films and their application in transistors. *J. Mater. Chem. C* **6**, 1393-1398, (2018).

36 Sanal, K. C. & Jayaraj, M. K. Room temperature deposited p-channel amorphous $Cu_{1-x}Cr_xO_{2-\delta}$ thin film transistors. *Appl. Surf. Sci.* **315**, 274-278, (2014).

37 Wang, L. *et al.* High-performance transparent inorganic-organic hybrid thin-film n-type transistors. *Nat. Mater.* **5**, 893-900, (2006).

38 Han, S. Y., Herman, G. S. & Chang, C. H. Low-temperature, high-performance, solution-processed indium oxide thin-film transistors. *J. Am. Chem. Soc.* **133**, 5166-5169, (2011).

39 Nayak, P. K., Hedhili, M. N., Cha, D. & Alshareef, H. N. High performance In_2O_3 thin film transistors using chemically derived aluminum oxide dielectric. *Appl. Phys. Lett.* **103**, 033518, (2013).

40 Lee, J. S., Kwack, Y.-J. & Choi, W.-S. Inkjet-printed In_2O_3 thin-film transistor below 200°C. *ACS Appl. Mater. Interfaces* **5**, 11578-11583, (2013).

41 Liu, A. *et al.* Fully solution-processed low-voltage aqueous In_2O_3 thin-film transistors using an ultrathin ZrO_x dielectric. *ACS Appl. Mater. Interfaces* **6**, 17364-17369, (2014).

42 Leppäniemi, J., Huttunen, O.-H., Majumdar, H. & Alastalo, A. Flexography-printed In_2O_3 semiconductor layers for high-mobility thin-film transistors on flexible plastic substrate. *Adv. Mater.* **27**, 7168-7175, (2015).

43 Ding, Y. *et al.* High-performance indium oxide thin-film transistors with aluminum oxide passivation. *IEEE Electron Device Lett.* **40**, 1949-1952, (2019).

44 Presley, R. E. *et al.* Tin oxide transparent thin-film transistors. *J. Phys. D: Appl. Phys.* **37**, 2810-2813, (2004).

45 Cheong, W.-S., Yoon, S.-M., Hwang, C.-S. & Chu, H. Y. High-mobility transparent SnO_2 and ZnO–SnO_2 thin-film transistors with SiO_2/Al_2O_3 gate insulators. *Jpn. J. Appl. Phys.* **48**, 04C090, (2009).

46 Jang, J. *et al.* Transparent high-performance thin film transistors from solution-processed SnO_2/ZrO_2 gel-like precursors. *Adv. Mater.* **25**, 1042-1047, (2013).

47 Jo, K.-W., Moon, S.-W. & Cho, W.-J. Fabrication of high-performance ultra-thin-body SnO_2 thin-film transistors using microwave-irradiation post-deposition annealing. *Appl. Phys. Lett.* **106**, 043501, (2015).

48 D.M, P., Mannam, R., Rao, M. S. R. & DasGupta, N. Effect of annealing ambient on SnO_2 thin film transistors. *Appl. Surf. Sci.* **418**, 414-417, (2017).

49 Lee, W. Y. *et al.* Densification control as a method of improving the ambient stability of sol-gel-processed SnO_2 thin-film transistors. *IEEE Electron Device Lett.* **40**, 905-908, (2019).

50 Shih, C. W., Yen, T. J., Chin, A., Lu, C. F. & Su, W. F. Low-temperature processed tinoxide transistor with ultraviolet irradiation. *IEEE Electron Device Lett.* **40**, 909-912, (2019).

51 Zhang, L. *et al.* Structural, chemical, optical, and electrical evolution of solution-processed SnO_2 films and their applications in thin-film transistors. *J. Phys. D Appl. Phys.* **53**, (2020).

52 Liang, D.-d., Zhang, Y.-q., Cho, H. J. & Ohta, H. Electric field thermopower modulation analyses of the operation mechanism of transparent amorphous SnO_2 thin-film transistor. *Appl. Phys. Lett.* **116**, 143503, (2020).

53 Carcia, P. F., McLean, R. S., Reilly, M. H. & Nunes, G. Transparent ZnO thin-film transistor fabricated by rf magnetron sputtering. *Appl. Phys. Lett.* **82**, 1117-1119, (2003).

54 Fortunato, E. M. C. *et al.* Fully transparent ZnO thin-film transistor produced at room temperature. *Adv. Mater.* **17**, 590-594, (2005).

55 Ong, B. S., Li, C., Li, Y., Wu, Y. & Loutfy, R. Stable, solution-processed, high-mobility ZnO thin-film transistors. *J. Am. Chem. Soc.* **129**, 2750-2751, (2007).

56 Lin, Y.-H. *et al.* High-performance ZnO transistors processed via an aqueous carbon-free metal oxide precursor route at temperatures between 80–180°C. *Adv. Mater.* **25**, 4340-4346, (2013).

57 Lin, Y.-Y., Hsu, C.-C., Tseng, M.-H., Shyue, J.-J. & Tsai, F.-Y. Stable and high-performance flexible ZnO thin-film transistors by atomic layer deposition. *ACS Appl. Mater. Interfaces* **7**, 22610-22617, (2015).

58 Saha, J. K. *et al.* Highly stable, nanocrystalline, ZnO thin-film transistor by spray pyrolysis using high-k dielectric. *IEEE Trans. Electron Devices* **67**, 1021-1026, (2020).

59 Yoon, M., Park, J., Tran, D. C. & Sung, M. M. Fermi-level engineering of atomic layer-deposited zinc oxide thin films for a vertically stacked inverter. *ACS Appl. Electron. Mater.* **2**, 537-544, (2020).

60 Kim, D. *et al.* Controllable doping and passivation of ZnO thin films by surface chemistry modification to design low-cost and high-performance thin film transistors. *Appl. Surf. Sci.* **509**, 145289, (2020).

61 Nomura, K. *et al.* Room-temperature fabrication of transparent flexible thin-film transistors using amorphous oxide semiconductors. *Nature* **432**, 488-492, (2004).

62 Yabuta, H. *et al.* High-mobility thin-film transistor with amorphous $InGaZnO_4$ channel fabricated by room temperature rf-magnetron sputtering. *Appl. Phys. Lett.* **89**, 112123, (2006).

63 Cho, Y.-J., Shin, J.-H., Bobade, S. M., Kim, Y.-B. & Choi, D.-K. Evaluation of Y_2O_3 gate insulators for a-IGZO thin film transistors. *Thin Solid Films* **517**, 4115-4118, (2009).

64 Chiu, C. J., Chang, S. P. & Chang, S. J. High-performance a-IGZO thin-film transistor using Ta_2O_5 gate dielectric. *IEEE Electron Device Lett.* **31**, 1245-1247, (2010).

65 Hsu, H., Chang, C. & Cheng, C. A flexible IGZO thin-film transistor withv stacked TiO_2-based dielectrics fabricated at room temperature. *IEEE Electron Device Lett.* **34**, 768-770, (2013).

66 Xu, W. *et al.* Low temperature solution-processed IGZO thin-film transistors. *Appl. Surf. Sci.* **455**, 554-560, (2018).